A hybrid method for airway segmentation and automated measurement of bronchial wall thickness on CT

Ziyue Xu [a], Ulas Bagci [b,*], Brent Foster [a], Awais Mansoor [a], Jayaram K. Udupa [c], Daniel J. Mollura [a]

[a] Center for Infectious Disease Imaging (CIDI), Radiology and Imaging Science Department, National Institutes of Health (NIH), Bethesda, MD 20892, United States
[b] Center for Research in Computer Vision (CRCV), Department of Computer Science, University of Central Florida (UCF), Orlando, FL 32816, United States
[c] Department of Radiology, University of Pennsylvania, Philadelphia, PA 19104, United States

ARTICLE INFO

ABSTRACT

Inflammatory and infectious lung diseases commonly involve bronchial airway structures and morphology, and these abnormalities are often analyzed non-invasively through high resolution computed tomography (CT) scans. Assessing airway wall surfaces and the lumen are of great importance for diagnosing pulmonary diseases. However, obtaining high accuracy from a complete 3-D airway tree structure can be quite challenging. The airway tree structure has spiculated shapes with multiple branches and bifurcation points as opposed to solid single organ or tumor segmentation tasks in other applications, hence, it is complex for manual segmentation as compared with other tasks. For computerized methods, a fundamental challenge in airway tree segmentation is the highly variable intensity levels in the lumen area, which often causes a segmentation method to leak into adjacent lung parenchyma through blurred airway walls or soft boundaries. Moreover, outer wall definition can be difficult due to similar intensities of the airway walls and nearby structures such as vessels. In this paper, we propose a computational framework to accurately quantify airways through (i) a novel hybrid approach for precise segmentation of the lumen, and (ii) two novel methods (a spatially constrained Markov random walk method (pseudo 3-D) and a relative fuzzy connectedness method (3-D)) to estimate the airway wall thickness. We evaluate the performance of our proposed methods in comparison with mostly used algorithms using human chest CT images. Our results demonstrate that, on publicly available data sets and using standard evaluation criteria, the proposed airway segmentation method is accurate and efficient as compared with the state-of-the-art methods, and the airway wall estimation algorithms identified the inner and outer airway surfaces more accurately than the most widely applied methods, namely full width at half maximum and phase congruency.

1. Introduction

Airways are the air-conducting structures (bronchi and bronchioles) bringing air into and out of the lungs from sites of gas exchange (alveoli). These airways comprise a complex and highly variable set of bifurcating structures having a tree-like configuration in the lungs. Airways are pathologically involved in various lung diseases. As examples, bronchiectasis is the dilation of airways (enlarged lumen), often resulting from chronic infection (Bagci et al., 2012a), obstruction, and inflammation. Airway wall thickening can be associated with airway narrowing, such as asthma and bronchitis. Tumors on airway walls can also form obstructions (Hansell et al., 2008).

CT imaging provides in-vivo anatomical information of lung structures in a non-invasive manner, which enables a quantitative investigation of airway pathologies. In conventional clinical settings, assessment of the airways is performed on CT slices at limited locations. Due to the inherent complexity of airway structures and the resolution limitations of CT, manually tracing and analyzing airways is an extremely challenging task, taking more than 7 h of intensive work per image (Sonka et al., 1996). Moreover, manual analysis suffers from large variability and low reproducibility especially for higher order branches. A precise method for segmentation of airways and an accurate estimation of airway walls may facilitate better quantification of airway pathologies, further enhancing the understanding of the mechanisms of disease progression.

Prior work: Many airway lumen segmentation approaches have been proposed and subsequently investigated in the literature, including rule-based (Sonka et al., 1996), morphology-based (Aykac et al., 2003), classification-based (Lo et al., 2010), etc. Among these methods, region growing (RG) is a widely used technique for identification of the airways. However, a simple intensity based RG strategy usually leaks into lung parenchyma often through blurred/broken

* Corresponding author. Tel.: +1407 823 1047.
 E-mail address: ulasbagci@gmail.com, bagci@crcv.ucf.edu (U. Bagci).

boundaries at small airways. RG can be considered reliable when analyzing large airway branches, including trachea and principal bronchi, however, the incorporation of higher level information is needed to identify smaller airways without leakage. Many studies have taken this approach recently. Alternatively, gray-scale morphological reconstruction (Aykac et al., 2003) has been shown to be effective for accurately identifying candidate airways on 2-D CT slices, but apart from being limited to 2-D cross sections, it does not yield high sensitivity when the airway is not perpendicular to the slice plane. Another approach for a better airway identification strategy is based on the enhancement of the tubular structures (i.e., vesselness filter) (Frangi et al., 1998). Although this process can further help identify small airway locations, it also yields unavoidable false positives over the lung area. Most of the previous methods made use of single enhancement only due to the challenge of combining the strength of different enhancement strategies. A detailed review on those methods with single enhancement as well as other computerized methods for identification and analysis of airways can be found in (Pu et al., 2012). Although comparison of the available methods in image segmentation literature is a challenging and subjective issue, recent attempts for direct comparison of several methods using the same image sets and reference standards make the direct comparison possible. Regarding airway extraction from CT scans, in particular, EXACT'09 (Lo et al., 2012) airway extraction challenge provides an objective platform for comparing airway extraction algorithms using a common dataset and performance evaluation method. In our study, we also use EXACT'09 challenge data for comparing our method with others.

Accurate measurement of airway wall dimensions has remained a challenge in particular because the outer wall characterization is often compromised by surrounding parenchyma and vessels. There have been many attempts in the literature to accurately measure airway structures and walls, we only explain the two most widely applied techniques herein, full width at half maximum (FWHM) (Amirav et al., 1993) and phase congruency (Estepar et al., 2006). FWHM defines the wall boundary at the location where the intensity is half the peak value. However, as shown in Reinhardt et al. (1997), the measurement can be biased due to partial volume effect and CT reconstruction algorithm. Furthermore, with the presence of adjacent vessels, the FWHM criterion may leak to surrounding structures. Algorithms have been proposed to improve the performance of FWHM, such as modeling the point spread function (Reinhardt et al., 1997) and applying elliptical correction (Saba et al., 2003). Phase congruency (Estepar et al., 2006), on the other hand, was conceived as a model-free alternative with edge locations identified by maximal local phase coherency. This method is shown to be robust; however, it is computationally intensive and accuracy for detection of small airways is limited by resolution. Recently, an increasing number of algorithms have begun to focus on 3-D methods that are potentially more efficient and perform better in complex branching areas. For instance, graph-based methods (Liu et al., 2013; Petersen et al., 2011) make use of new voxel re-sampling techniques to extract non-intersecting columns that are suitable for airway wall geometry. A 3-D active surface evolution approach (Gu et al., 2013; Ortner et al., 2011) is utilized to initialize a 3-D deformable model inside the airway, which further evolves under predefined external and internal forces automatically to reach the wall location. To assess the performance of the wall segmentation methods, phantoms with known diameters were often used. However, such phantoms usually fail to simulate the appearance of airways in a realistic manner with complex surroundings of blood vessels and lung parenchyma. Alternatively, as a common practice for segmentation evaluation, the performance of the wall segmentation methods can be assessed with regard to the manual references and compared with the basic FWHM method. In this paper, not only we used publicly available EXACT'09 challenge data but we also used reference standards which were manually obtained from expert radiologists for evaluating our methods.

Fig. 1 illustrates the flowchart of our proposed scheme. First, we segment the lumen area (Fig. 1B) of the airway from CT scans (Fig. 1A) using a novel multi-scale hybrid approach based on fuzzy connectedness (FC) (Udupa and Samarasekera, 1996) image segmentation. The proposed method designs the FC machinery with a predefined *fuzzy affinity* relationship. This relationship is very versatile and convenient for combining multiple strategies to restrict the segmentation procedure to only airway regions and achieves *high sensitivity* with lower leakage. Once airway lumen is segmented, we extract the tree skeleton from the binary image using a thinning algorithm (Ibanez et al., 2005) and refine the resulting skeleton using a graph-based dynamic programming method (Fig. 1C). Next, we apply two methods for airway wall estimation: a 3-D method based on constrained relative fuzzy connectedness (RFC) (Saha and Udupa, 2001) that is more efficient and better handles branching geometry, and a 2-D method based on constrained random walk (RW) that suits better with current clinical practice. For RFC, a 3-D seeding scheme that defines three surfaces: (i) inside lumen, (ii) within wall, and (iii) outside wall, is first applied for constraining 3-D RFC computation (Fig. 1D1). Then RFC is performed using the three seed sets to determine the airway wall region (Fig. 1E1). For RW, 2-D orthogonal samples are first generated along every branch of the airway skeleton (Fig. 1D2). On the 2-D orthogonal images (Fig. 1E2), FWHM is first performed to roughly identify the range of the lumen, the airway wall, and the parenchyma (Fig. 1F2); an ellipse fitting process is then added to improve estimation (Fig. 1G2). Seeds (Fig. 1H2) for the lumen, airway wall, and parenchyma are determined automatically to initiate random walk segmentation (Fig. 1I2).

Preliminary versions of the proposed methods were presented at MICCAI 2013 (Xu et al., 2013a) and ISBI 2013 (Xu et al., 2013b). To summarize our contributions, we have developed a framework for accurate, robust, and fast airway quantification which includes wall thickness estimation as well as airway tree extraction (lumen). For airway lumen segmentation, we combined the two enhancement methods, i.e., gray-scale morphological reconstruction and multi-scale vesselness, for their effective intensity and object scale modeling under the FC segmentation framework. We showed that FC is a remarkably suitable platform for combining strengths of such techniques, as also its effectiveness is verified through the experimental results. For airway wall segmentation, we provided a spatially constrained RW solution for pseudo 3-D analysis, and a RFC method in 3-D analysis, that successfully avoided leakages into neighboring structures. In the next section, we present our proposed framework in detail.

2. Methods

2.1. Airway lumen segmentation

We design a novel *fuzzy affinity* relationship to tailor the FC segmentation (Udupa and Samarasekera, 1996) to airway regions by using multiple strategies in order to achieve *high sensitivity* and low leakage. Fig. 2 illustrates the flowchart representation of the proposed method of airway lumen segmentation. First, a seed is identified in the trachea automatically by 2-D Hough transform, then, two tubular structure enhancement techniques are performed on the CT images simultaneously: a gray-scale morphological reconstruction (Aykac et al., 2003) operation, and a vesselness (Frangi et al., 1998) computation. The two enhanced images are further passed together with the seed to the FC computation of the airway lumen. Our motivation for this combination within the FC framework is to help identify the airway structures and provide continuity of the lumen boundary.

2.1.1. Gray-scale morphological reconstruction

In pulmonary CT images, the airway can be regarded as the local minima of intensity in a 2-D slice I that can be enhanced by applying
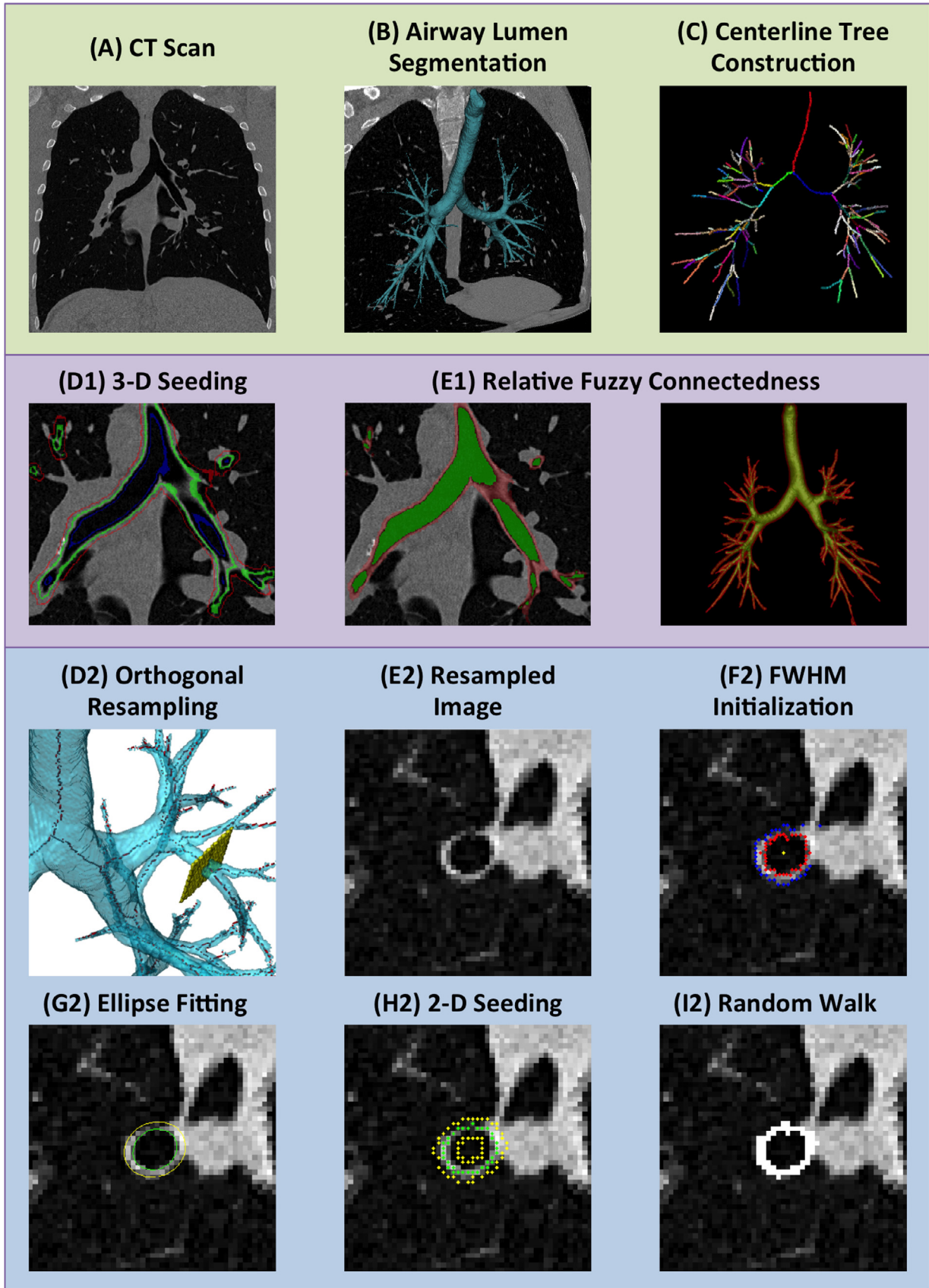
Fig. 1. Flowchart of the airway lumen segmentation and wall estimation algorithms with (1) 3-D relative fuzzy connectedness and (2) 2-D random walk.
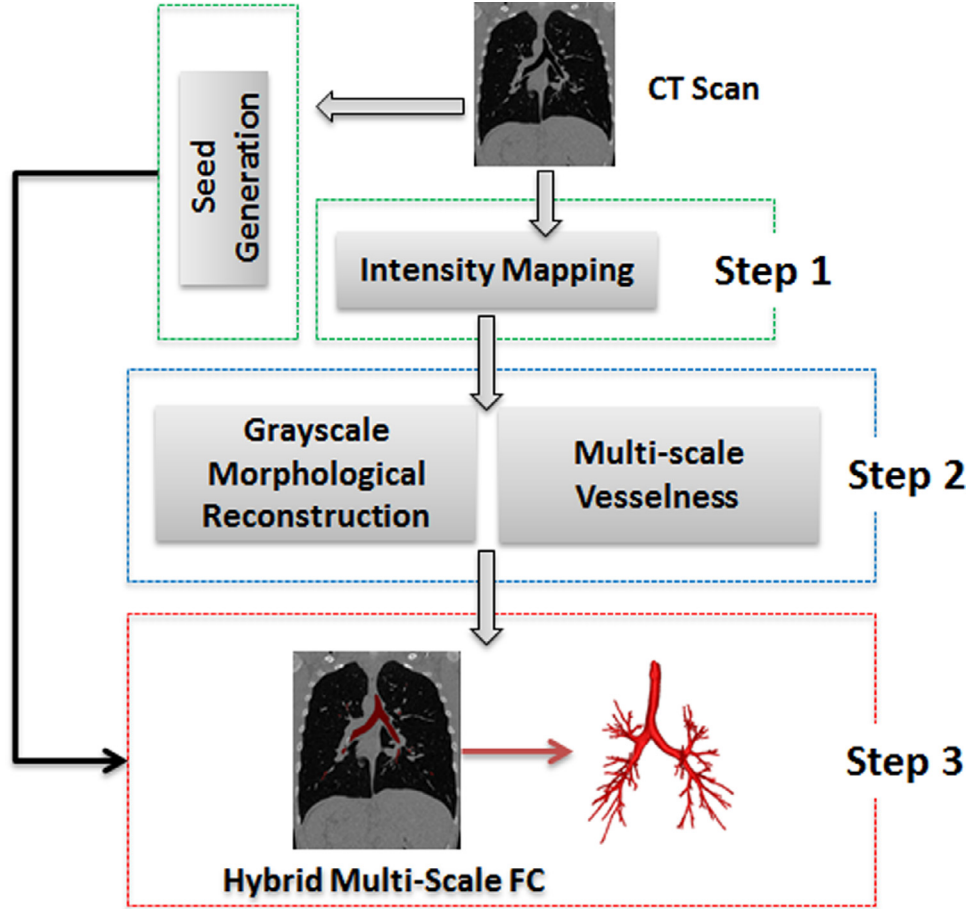
Fig. 2. Flowchart of the airway lumen segmentation algorithm.

gray-scale morphological reconstruction. Airways of different diameters are handled using a range of morphological structuring elements (SE) by successive dilation on the basis of SE as

$$B_n = B_0 \oplus B_0 \oplus \cdots \oplus B_0, \tag{1}$$

where B_0 is the smallest four neighborhood binary SE, B_n is the n times dilation result of B_0, and $\oplus$ is the dilation operator.

A "marker image" (Aykac et al., 2003) is then constructed from the original image slice I and SE B_n by a gray-scale closing operation $\bullet$ as

$$J_1^n = I \bullet B_n \triangleq (I \oplus B_n) \ominus B_n, \tag{2}$$

where $\ominus$ is the erosion operator. Further, a recursive process is performed on J_1^n as $J_{k+1}^n = \max(J_k^n \ominus B_0, I)$ until no changes occur within an iteration which results in the final gray-scale reconstructed image J_∞^n for SE B_n.

In J_∞^n, the local minima smaller than B_n are filled in with a value proportional to the difference between max and min values within the neighborhood B_n. Therefore, the difference image $D = J_\infty^n - I$ identifies potential airway locations and the process is completed by combining maximum responses from different SEs.

2.1.2. Multi-scale vesselness enhancement

Vessel enhancement algorithms are often employed to improve vascular structure identification and delineation. As shown (Frangi et al., 1998), analyzing the second-order information (Hessian) of a Gaussian convolved image provides local information of the structure. Specifically, eigenvalue decomposition is performed over the Hessian matrix and the resulting ordered eigenvalues, i.e., $(|\lambda_1| \leq |\lambda_2| \leq |\lambda_3|)$, are examined. For voxels within vessels in particular, it is expected that λ_1 is small, while the other two are large and of equal

sign that indicates whether the vessel is brighter or darker than background. Explicitly, the vesselness can be formulated as

$$V_\sigma = \begin{cases} 0, & \text{if } \lambda_2 > 0 \text{ or } \lambda_3 > 0; \\ (1 - e^{-\frac{R_A^2}{2\alpha^2}})e^{-\frac{R_B^2}{2\beta^2}}(1 - e^{-\frac{S^2}{2\gamma^2}}), & \text{otherwise,} \end{cases} \tag{3}$$

for a bright vessel on dark background, and $R_A = |\lambda_2|/|\lambda_3|$, $R_B = |\lambda_1|/|\lambda_2\lambda_3|$ and $S = \sqrt{\lambda_1^2 + \lambda_2^2 + \lambda_3^2}$. The vesselness measure above is calculated at different scales (σ), and the maximum response is achieved at a scale that matches the size of the vessel. Therefore, by using a multi-scale approach which covers a range of vessel widths and finding the maximum value $V = \max(V_\sigma)$, $\sigma_{\min} \leq \sigma \leq \sigma_{\max}$, we get the vesselness measure as well as the approximate local vascular structure scale for each voxel in the image.

2.1.3. Affinity relations and hybrid modeling of FC

Our motivation to incorporate vesselness filtering (Frangi et al., 1998) and gray-scale morphological reconstruction (Aykac et al., 2003) within the FC framework was to help identify the airway structures and provide information for keeping the continuity of the airway boundary. See Fig. 3 for an example image of airway enhancement. Note that a simple intensity based affinity relation may cause leakage due to blurred and soft boundaries (Fig. 3A); gray-scale morphological reconstruction enhances the airway lumen, but due to its 2-D nature, it is inhomogeneous along 3-D structure (Fig. 3B), and vesselness computation results in false positives over the image (Fig. 3C). Herein, we combine complementary strengths of these measures within the FC framework as FC has the ability to combine different features within the same formulation. Next, we explain this formulation briefly.
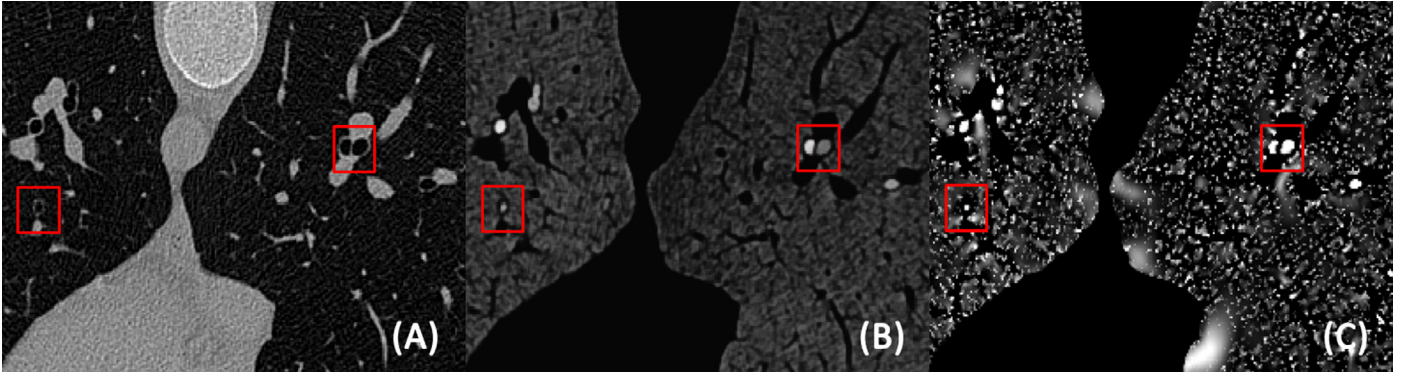
Fig. 3. Airway lumen enhancement (A) original image, (B) gray-scale morphological reconstruction result, and (C) vesselness computation result.

In the FC framework, a fuzzy topological construct characterizes how voxels of an image hang together to form an object through a predefined function called *affinity* (Saha and Udupa, 2001). Assuming $\mathcal{V} \subset \mathbb{Z}^3$ denotes a 3-D cubic grid representing the *image space*, where each element of $\mathcal{V}$ is called a *voxel*, a topology on an image is given in terms of an *adjacency* relation (μ_α) such that the adjacency relation is a binary relation on the image and it determines which pairs of voxels are close enough to be considered connected: $\mu_\alpha : \mathcal{V} \times \mathcal{V} \to \{0, 1\}$. Theoretically, if p and q are α-adjacent to each other, then $\mu_\alpha(p, q) = 1$, '0' otherwise. In practice, we set $\alpha = 26$ for adjacency in 3-D analysis. While affinity is intended to be a local relation, a global fuzzy relation called fuzzy connectedness is induced on the image domain by the affinity functions. This is done by considering all possible paths between any two voxels p and q in the image domain, and assigning the strength of fuzzy connectedness to each path. The level of the fuzzy connectedness between any two voxels p and q is considered to be the maximum of the strengths of all paths between p and q.

An *affinity relation* κ is the most fundamental measure of local hanging togetherness of nearby voxels. For a path π, which is a sequence of voxels $\langle p_1, p_2, \ldots, p_l \rangle$ with every two successive voxels being adjacent, given *fuzzy affinity function* $\mu_\kappa(p_i, p_{i+1})$, the strength of the path is defined as the minimum affinity along the path:

$$\mu_{\mathcal{N}}(\pi) = \min_{1 \le i < l} \mu_\kappa(p_i, p_{i+1}). \tag{4}$$

Then, the strength of connectedness $\mu_\kappa(p, q)$ between any two voxels p and q is the strength of the strongest path between them as

$$\mu_{\mathcal{K}}(p, q) = \max_{\pi \in \mathcal{P}(p,q)} \mu_{\mathcal{N}}(\pi), \tag{5}$$

where $\mathcal{P}(p, q)$ denotes the set of all paths between p and q. Therefore, a fuzzy connected object $\mathcal{O}$ in an image can be defined for a predetermined set of seeds S. Since the level of FC between any two voxels p and q is considered to be the maximum of the strengths of all paths between them, for multiple seeds, the fuzzy object membership function for $\mathcal{O}$ or the strength of connectedness of $\mathcal{O}$ is defined as follows:

$$\mu_{\mathcal{O}}(p) = \max_{s \in S} \mu_{\mathcal{K}}(p, s). \tag{6}$$

An efficient computational solution is presented (Udupa and Samarasekera, 1996) for computing $\mu_{\mathcal{O}}(p)$, given κ and S and an image.

Effectiveness of the FC algorithm depends on the choice of the affinity function. The most prominent affinities used so far are a combination of: (i) adjacency-based μ_α, (ii) homogeneity-based μ_ψ, and (iii) object feature-based μ_ϕ such that fuzzy affinity is defined as

$$\mu_\kappa(p, q) = \begin{cases} 1, & \text{if } p = q; \\ \mu_\alpha(p, q)\sqrt{\mu_\psi(p, q)\mu_\phi(p, q)}, & \text{otherwise,} \end{cases} \tag{7}$$

where $\mu_\psi(p, q)$ captures the homogeneity between p and q, with a higher value for pairs with similar intensity. For object feature-based

affinity, $\mu_\phi(p, q)$ defines the hanging-togetherness of p and q in the target object based on the nearness of their feature values to the expected feature distribution of the target object. The affinity function can be formulated differently depending on the specific objective. Besides the common adjacency term, one can choose to use homogeneity, or object feature, or both. When using both, the square root is taken to ensure the same value range with other settings. The general form of $\mu_\psi(p, q)$ and $\mu_\phi(p, q)$ are

$$\mu_\psi(p, q) = e^{-\frac{|f(p)-f(q)|^2}{2\sigma_\psi^2}}, \tag{8}$$

$$\mu_\phi(p, q) = \min\left(e^{-\frac{|f(p)-m|^2}{2\sigma_\phi^2}}, e^{-\frac{|f(q)-m|^2}{2\sigma_\phi^2}}\right), \tag{9}$$

where σ_ψ and σ_ϕ are two different standard deviation parameters used for homogeneity and object feature distribution, m is the mean object feature value, and f denotes image intensity function: $f : \mathcal{V} \to \mathcal{L} \subset \mathbb{Z}$. For intensity, m can be obtained directly from the standard HU value for different tissue/subject types, such as -1000 for air. More precisely and for the two enhancements, m can be estimated using user-defined ROI for target object. Regarding the influence of seed locations and amount, FC is known for its robustness under different seed parameters compared to other seed based segmentation algorithms.

For the algorithm discussed here, three features are available to describe a given voxel x: intensity $I(x)$, gray-scale morphological reconstructed result $D(x)$, and vesselness measurement $V(x)$ such that $F(x) = (I(x), D(x), V(x))$. Moreover, the local scale information, $ls(x)$, provided by the multi-scale vesselness computation, gives additional control over the design of the affinity function since sole intensity information is not highly reliable for small airway identification; the other two features yield support. Therefore, affinities $\mu_{\psi/\phi}^I$, $\mu_{\psi/\phi}^D$, and $\mu_{\psi/\phi}^V$ corresponding to $I(x)$, $D(x)$ and $V(x)$ can be combined through the local scale measure as:

$$\mu_{\psi/\phi}^{\text{FC}} = \begin{cases} \mu_{\psi/\phi}^I, & \text{if } ls > ls^{\max}; \\ k\mu_{\psi/\phi}^I + (1-k)\sqrt{\mu_{\psi/\phi}^D \mu_{\psi/\phi}^V}, & \text{otherwise,} \end{cases} \tag{10}$$

where $ls^{\max}$ is the threshold for determining large airways, for which intensity is reliable, and k is a weighing parameter, $k \in [0, 1]$. For our experiment, we have used the widely accepted 2 mm as the threshold for small airways. Since intensity plays a less important role for finer structures, k may be formulated as $k = ls/ls^{\max}$. In other words, $\mu_{\psi/\phi}^{\text{FC}}$ is a piecewise function which controls selection of both large and small airways.

Briefly, in order to obtain a binary segmentation of the lumen with the presented affinities, we employ the following steps. First, one or more seeds at trachea are identified with Hough transform. Second, pairwise FC of all other voxels with regard to the seeds are computed
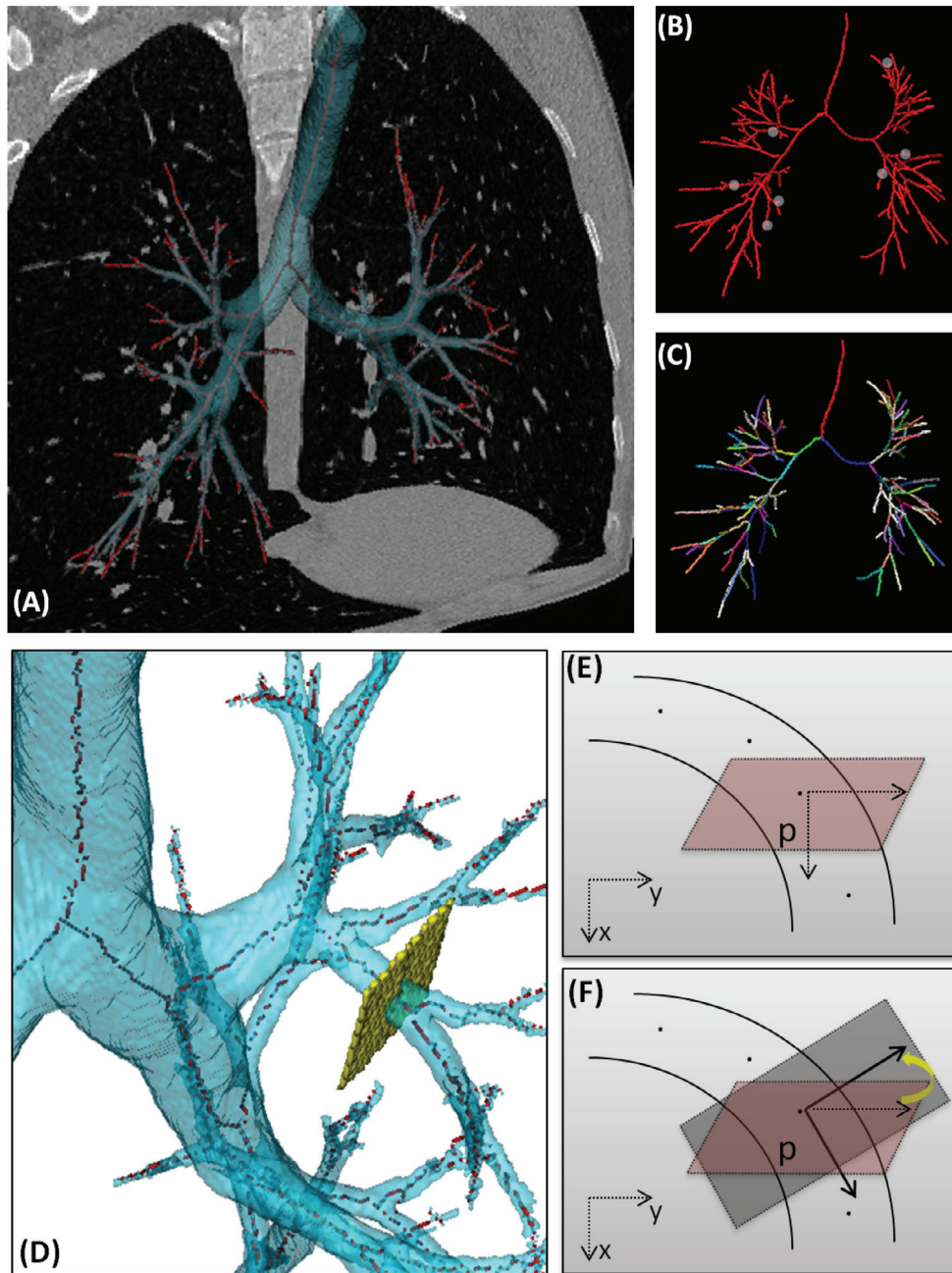
Fig. 4. (A) Segmented lumen (green) and its centerline (red). (B) Redundant structures over centerlines are seen prior to pruning-thinning process. (C) Thinning removes the redundant structures and each branch is labeled. (D) Orthogonal plane at a skeleton point. (E) Slice plane that may not be perpendicular to local tangent vector. (F) Orthogonal resampling. (For interpretation of the references to color in this figure legend, the reader is referred to the web version of this article.)

following Eqs. (4)–(6), where affinity is formulated as in Eq. (7) with combined information as in Eq. (10). Each component in Eq. (10) is calculated from Eqs. (8) and (9). Third, the resulting FC map describes the strength of the connection between every voxel to the seeds, so a binary segmentation can be extracted by thresholding the FC map.

2.2. Centerline extraction and orthogonal resampling

Centerline extraction of the lumen is a necessary step for airway wall identification and description of 3-D airway geometry. The tree skeleton is extracted from the segmented lumen using a binary thinning algorithm (Ibanez et al., 2005) (Fig. 4A). To generate a systematic description of the airway tree, we divide the 3-D skeleton into individual branch segments at every branching point. Since

the tree produced by the thinning algorithm often contains small false branches corresponding to local morphological variation, rather than real branching (Fig. 4B), a graph-based dynamic programming method is employed to optimally prune the resulting tree by removing the small branches (Fig. 4C), which is similar to the optimization used in literature (Xu et al., 2012). Assuming each branch segment is represented as a node in the graph, its maximum length L to the leaf nodes is found by dynamic programming. If L and/or the ratio with its brother node, L/L_{bro}, is below a preset threshold, then the node and its children are removed from the tree. Finally, smoothing is performed on each segment to avoid sharp changes in local tangent orientation along the skeleton. In practice, we have used $L = 5$ and $L/L_{bro} = 0.1$ for airway tree applications and observed satisfying results. The original CT image is then resampled into 2-D images over a small domain in
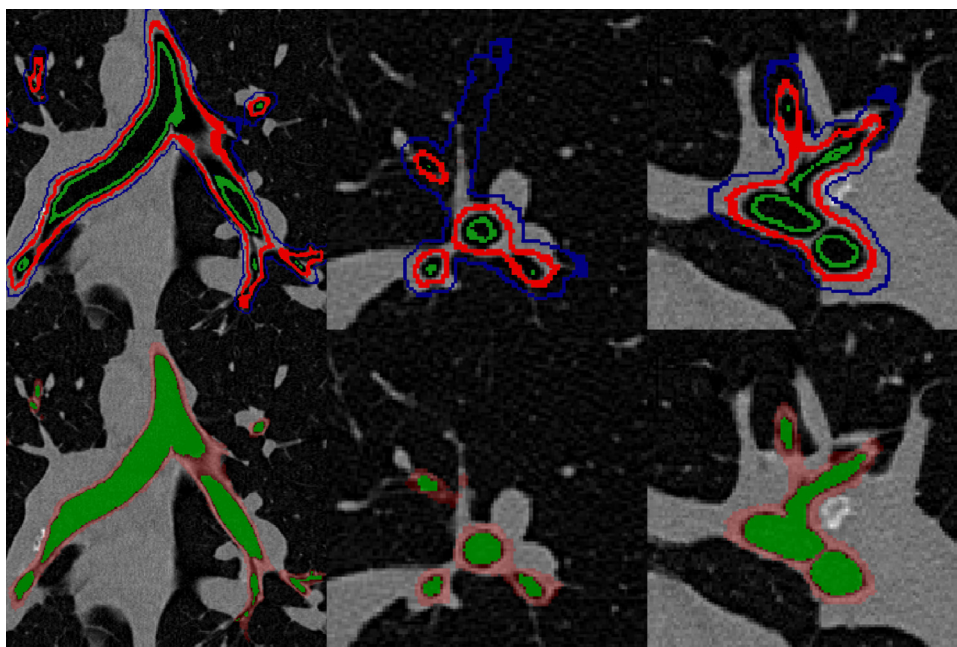
Fig. 5. First row: Airway walls with inside lumen (green), within wall (red), and outside the outer wall (blue) seeds. Second row: Resulting RFC segmentation with lumen (green) and walls (red). (For interpretation of the references to color in this figure legend, the reader is referred to the web version of this article.)

the orthogonal planes (Fig. 4D and F). Note that resampling is done on the plane perpendicular to the local tangent vectors (Fig. 4E and F).

2.3. Spatially constrained RFC for 3-D airway wall estimation

Absolute FC segmentation is based on computing the FC strength between a set of seed points and all other voxels within the image and set a proper threshold to the resulting FC image. On the other hand, RFC is based on several seed sets S_i, $i = 1, 2, \ldots, k$. FC strength is first computed at every voxel for each of the seed sets individually, and then the voxel is labeled as belonging the seed set with maximum FC value. In this way, the thresholding step is avoided. Specifically for the task of airway wall estimation, due to similar intensities of airway wall and nearby structures such as blood vessels, sparse seeding will result in fragmented segmentation and leakages. Therefore, a spatially constrained RFC method is developed for airway wall estimation. Similar to the 3-D active surface evolution approach (Gu et al., 2013; Ortner et al., 2011), three surfaces are first identified using the already segmented lumen region: inside the lumen, within the airway walls, and outside the outer wall. The surface inside the lumen is defined as the surface one voxel inside the segmented lumen region which is estimated using morphological erosion. With the extracted centerline, FWHM is first used to roughly identify the extent of surrounding airway wall at every skeleton point. Such estimation is further filtered and smoothed to get rid of noise for extracting the surface within the airway walls. The outer surface is subsequently defined by morphological dilation of the airway wall surfaces. Next, FC strength is computed using the three seed sets and the airway walls are identified based on RFC theorem. See Fig. 5 for an example of the surfaces obtained from seeding and the final segmentation results.

2.4. Spatially constrained Markov random walk for 2-D airway wall estimation

Routine clinical assessment of airway walls is based on 2-D examination of airways at limited locations. Furthermore, there have been controversies on the feasibility of using pseudo 3-D (slice-by-slice, where each slice is 2-D) and 3-D methods in the literature regarding

airway wall analysis. To address these issues, alternative to the fully 3-D RFC based method, we develop a novel fully automatic pseudo 3-D (i.e., slice-by-slice) method for quantifying airway walls based on random walk (RW) image segmentation. The RW algorithm has been a widely used graph-based image segmentation method (Grady, 2006). In RW, the image is considered a graph (G), which is represented as a pair, $G = (V, E)$, with nodes $v \in V$ and edges $e \in E \subseteq V \times V$. Conventionally, a node v_i is said to be a neighbor of another node, v_j, if they are connected by an edge e_{ij} in G, and each edge is weighted by w_{ij}. Basically, these weights denote the likelihood that a random walk will cross edges (Bagci et al., 2012b; 2013d). Although RW *usually* avoids the noisy or fragmented segmentation, it has been recently shown (Cheng and Zhang, 2011) that this property does not always hold. Similarly, in airway wall surface segmentation, fragmented segmentation can likely occur due to similar intensity profiles of the airway walls and the nearby structures; therefore, one needs to be sure to place an *adequate number* of seeds in *suitable places*. To avoid the "connectedness" problem and provide an accurate estimation of inner and outer wall surfaces, in this study we create a computationally efficient random walk estimation method by automatically identifying foreground and background seeds that spatially constrain random walkers (Xu et al., 2013a). The algorithm uses FWHM and ellipse fitting methods to *roughly* identify the foreground and background seed locations. FWHM is first applied to locate the double edges for airway wall, then ellipse fitting is used to smooth the result and compensate for missing information caused by adjacent vessel. After these two steps, the approximate airway inner and outer wall surfaces S_1^0 and S_2^0, as well as a estimation of overall airway wall thickness d_{wall}, can be roughly determined. For RW seeding, foreground seeds corresponding to airway wall are distributed halfway between S_1^0 and S_2^0; while background seeds corresponding to lumen (inside airway) and paranchyma/vessel (outside airway wall) are located on surfaces $S_1^{n_1}$ inside S_1^0 and $S_2^{n_2}$ outside S_2^0 respectively. Scale parameters n_1 and n_2 are used to define the location of two surfaces, such that the distance between $S_1^{n_1}$ and S_1^0 is $d_1 = n_1 \cdot d_{\text{wall}}$, and $S_2^{n_2}$ and S_2^0 is $d_2 = n_2 \cdot d_{\text{wall}}$.

Furthermore, foreground and background seeds are connected within each group so that they form 2-D convex bodies in the vicinity of outer and inner walls; therefore, hits-and-runs of random walks
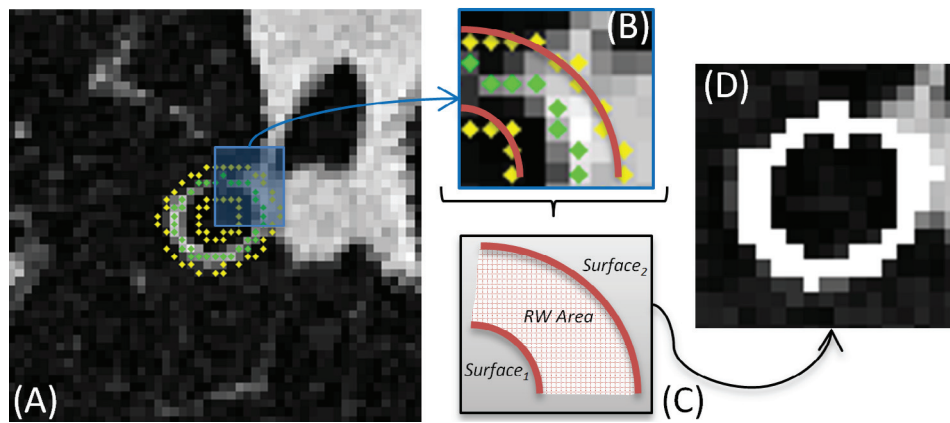
Fig. 6. (A) Airway wall with background (yellow) and foreground (green) seeds, and its zoomed version (B). (C) Background seeds form inner and outer surfaces as constraints for RW. (D) Resulting RW segmentation. (For interpretation of the references to color in this figure legend, the reader is referred to the web version of this article.)

are restricted to the no "connectedness" issue when it converges to outer and inner surface locations. Other than the automatically localized background and foreground seeds and their spatial alignment within the two ellipses (Fig. 6B), the rest of the combinatorial Drichlet problem was solved, as indicated (Grady, 2006). Note that although airway tree as a 3-D object is obviously not convex, the airway can be approximated as circles at local cross-sections. Hence, we used connected inner and outer seeds. Also, since each segmentation is performed within a small neighborhood around a centerline point, and every time the seed point are allocated independently, the seeds will not "conflicting" with each other. Thus the bifurcation is not a problem for the proposed method.

In conventional RW segmentation, the aim is to classify a large number of unlabeled voxels with a limited number of labeled voxels; however, herein, we classify a relatively small number of unlabeled voxels, with a large number of labeled voxels distributed over two convex surfaces (Fig. 6A–C). Our proposed framework allows random walkers to exploit the airway wall structures within two convex surfaces (S_1^0 and S_2^0) in a robust and computationally efficient way (see Fig. 6D). Distribution of seed sets and its connection to the soft constraint will be given in Section 3.

3. Experiments and results

3.1. Data

In the context of segmentation, the "gold standard" is usually not available (Bagci et al., 2013b). Instead, manual delineation is often used as the reference standard. However, for both airway lumen and wall segmentation, especially in the presence of pulmonary diseases, it is extremely labor intensive since not only does it take many hours to segment a single lung CT scan, but it is also necessary to have a large and diverse dataset that covers images under various conditions. Here, we used the data set from the "EXACT'09 airway lumen segmentation challenge" (Lo et al., 2012), including CT studies from 20 subjects. Lumen segmentation was performed with the proposed method, and the resulting binary segmentations were submitted to the organizers who sent the quantitative evaluations back. Unfortunately, for airway wall segmentation, there is no such open evaluation platform. Therefore, manual segmentations were used as references in validation. For this purpose, we selected 300 images that contained airways of different sizes under different imaging and anatomical conditions from the orthogonal resampled 2-D images generated from the EXACT'09 data set. All 2-D resampled images were first roughly grouped to large, medium, and small according to their size. Then, within each group, 100 samples were randomly selected for the test data set. Segmentations of these images were

produced by two independent experts (i.e., Observers 1 and 2) as surrogates of the ground truth. The 2-D resampled images were rescaled to 0–255 range using window level at − 450 HU with width 1500 HU as suggested in Okazawa et al. (1996) to "window" the airway anatomy for clinical purpose. In the following sections, all experimental results reported are based on the entire EXACT dataset for lumen segmentation, and all 300 2-D samples for wall segmentation.

3.2. Evaluation of lumen segmentation

To evaluate the performance of lumen segmentation, we submitted the binary results by the proposed method to the EXACT'09 organizers, and received the detailed quantitative measurements. In the following, we provided two qualitative examples, together with the overall quantitative results. More details, including 3-D rendering and evaluation measurements of each individual case, were listed in the Appendix.

Fig. 7 shows qualitative evaluation of our proposed method compared to two of the state-of-the-art methods. Here, we made our best effort to choose the same rendering scheme and 3-D viewing angles as the results provided by EXACT'09 for qualitative observation, although a minor misalignment may still be unavoidable. For comparison purposes, we selected the best method in the sense of highest tree length detection rate under the restriction of low false positive rate (FPR) (< 1%) which was suggested by the DIKU (Lo et al., 2009) group who hosted the challenge. Also, the result given by the UAVisionLab (Pinho et al., 2009) group was used as another reference since the quantitative difference between the UAVisionLab and our method is comparable to the difference between our method and the DIKU method. In the sense of algorithm complexity, UAVisionLab designed their method based on basic RG with a leakage control mechanism, while DIKU made use of vessel–airway relationship to formulate a more advanced voxel classification approach. The UAVisionLab method (A) detected tree length of 26.1% at an FPR of 1.14%; the DIKU group (B) detected tree length of 68.7% at an FPR less than 0.01%; and our result (C) achieved detected tree length of 48.6% and FPR of 0.19%. From the statistics, we noticed that the difference in detected tree length was about 20% with the difference between FPRs about 1 order of magnitude for both (A)–(C) and (B)–(C). However, as it visually appears, the difference between (B)–(C) is more subtle than that of (A)–(C). Given the fact that there is currently no consensus on the clinical contribution of airway morphometry over disease investigation, both visual and quantitative evaluations reveal partial information regarding the segmentation performance. The ultimate evaluation should include considerations of airway pathology and its clinical significance.
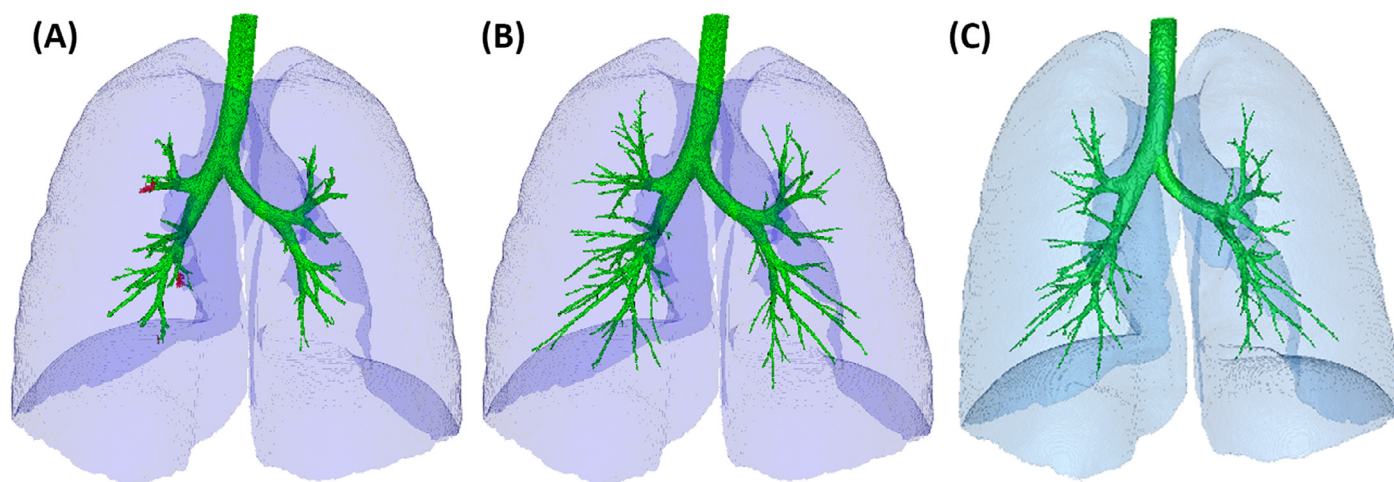
Fig. 7. 3-D Segmentation results on image CASE22 of EXACT'09 dataset (Lo et al., 2012). (A) Result produced by UAVisionLab with detected tree length 26.1% and false positive rate 1.14%. (B) Result produced by DIKU with detected tree length 68.7% and false positive rate less than 0.01%. (C) Result produced by our hybrid FC method with detected tree length 48.6% and false positive rate 0.19%. The red part in (A) shows the leakage. (For interpretation of the references to color in this figure legend, the reader is referred to the web version of this article.)
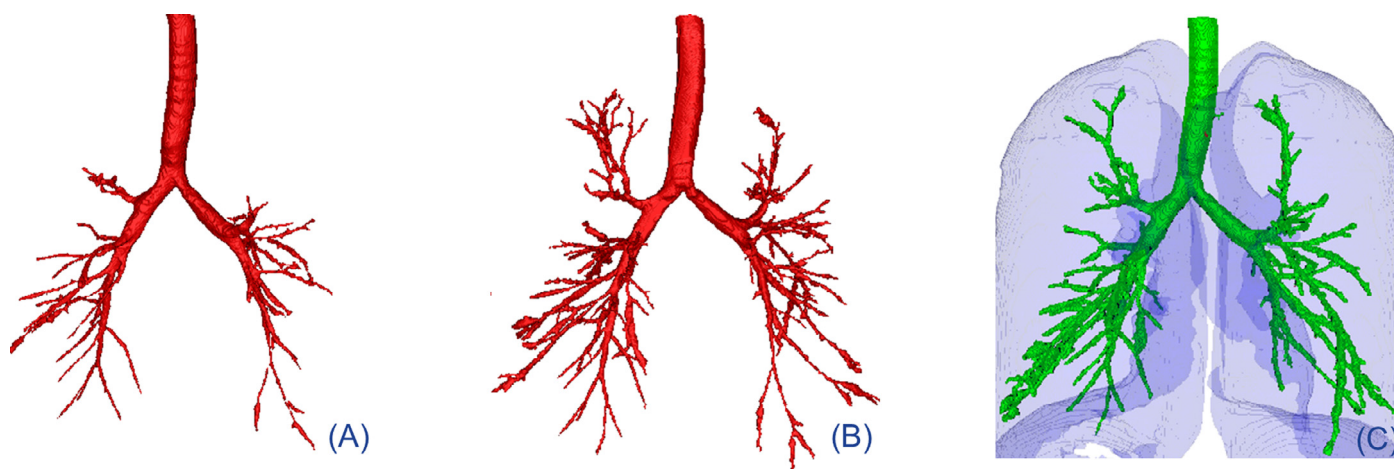

Fig. 8. 3-D Segmentation results on image CASE36 of EXACT'09 dataset (Lo et al., 2012). (A) Result submitted to organizer without parameter tuning with detected tree length 27.9%. (B) Result produced with parameter tuning. (C) Reference result by ARTEMIS-TMSP with detected tree length 62.6%.

Table 1
Results of accuracy analysis of airway segmentation given by EXACT'09. Statistics with respect to methods for comparison (UAVisionLab and DIKU) are given for overall performance (AVG: mean and STD: standard deviation) as well as an example case of CASE22 as shown in Fig. 7.

		Branch count	Branch detected (%)	Tree length (cm)	Tree length detected (%)	Leakage count	Leakage volume (mm^3)	False positive rate (FPR) (%)
UAVisionLab	AVG	74.2	32.1	51.9	26.9	4.2	430.4	3.63
	STD	29.5	6.9	19.6	6.9	4.4	672.3	4.92
	CASE22	132	34.1	86.4	26.1	7	160.0	1.14
Proposed	AVG	128.68	51.74	94.81	44.52	8.63	121.37	0.85
	STD	60.29	10.84	44.70	9.39	10.74	292.21	1.59
	CASE22	210	54.3	160.6	48.6	7	26.5	0.19
DIKU	AVG	150.4	59.8	118.4	54.0	1.9	18.2	0.11
	STD	85.2	13.6	75.4	13.4	3.9	48.0	0.22
	CASE22	276	71.3	227.1	68.7	1	0.2	< 0.01

For a more in-depth evaluation, Table 1 summarizes the statistics of the results, as compared with the two reference methods with overall performance and specific case of CASE22 as shown in Fig. 7. Statistics of each individual cases are listed in the Appendix, and detailed descriptions of individual evaluation parameters are available in EXACT'09 (Lo et al., 2012). It also worth mentioning that the submitted results were generated using the same parameters and no parameter-tuning was applied. To further illustrate the capability of the proposed method, we have optimized the parameter for CASE36, which yields the lowest detection rate of 27.9% initially with respect to the other cases. In Fig. 8, (A) shows the submitted result without parameter tuning, (B) presents the result with parameter tuning, and (C) shows a reference result from ARTEMIS-TMSP (Fetita et al., 2009), which has the highest detected tree length. As can be observed, after parameter tuning, the proposed method captures similar amount of, if not more, details as compared with the reference method, which achieves a detection rate of 62.6%.

Our proposed method takes approximately 20 min for each test image. In the presented approach, the time for computationally involved gray-scale morphological reconstruction is decreased by using
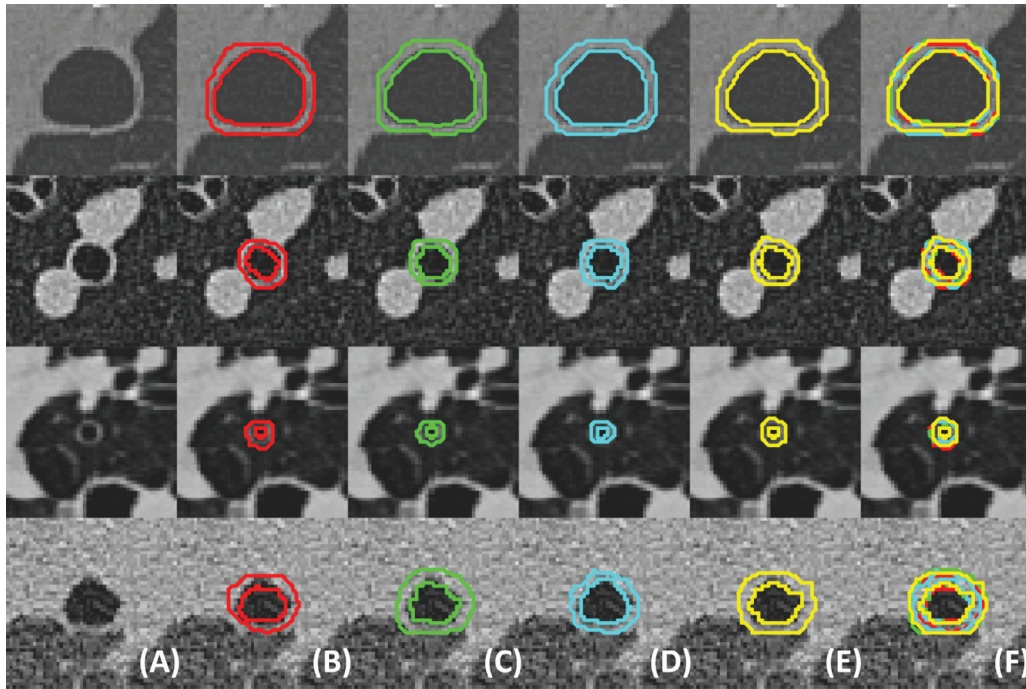
Fig. 9. Airway wall estimation result for airways of different sizes and under different anatomical conditions. (A) Original image, (B), (C) two manual segmentation results, and results from the proposed 2-D RW method (D) and 3-D RFC method (E), the last column illustrates the fused results (F). (For interpretation of the references to color in the text, the reader is referred to the web version of this article.)

Table 2
Features of 300 samples for testing according to lumen diameter, contrast, SNR, and well-defined wall percentage.

Diameter	Percentage	Contrast	Percentage	SNR	Percentage	Well-defined wall	Percentage
Small	43%	< 5	20%	< 2	9%	< 25%	10%
MediumLow	20%	5–10	28%	2–3	48%	25%–50%	16%
MediumHigh	27%	10–20	39%	3–4	32%	50%–75%	43%
Large	10%	> 20	13%	> 4	11%	> 75%	31%

a multi-scale approach. In addition, our method does not require any training process, which can be time consuming considering the need for precise manual segmentations. The computational efficiency can be further improved by code optimization and multithreaded/parallel computation. Visually, we found subtle differences while comparing the top ranked methods, including ours. Indeed, our method exhibited a much higher efficiency (20 min) than the top ranked method (90 min) in terms of the computational burden.

3.3. Evaluation of airway wall surface estimation

To evaluate the performance of airway wall segmentation against manual references from 300 2-D samples, Dice similarity coefficients (DSCs) and Hausdorff distances (HDs) were calculated and accompanied by inter-observer agreement rate as a convention. Fig. 9 provides 4 examples from the test data set, with corresponding two manually drawn boundaries (red and green) and estimations by the proposed 2-D RW method with $n_1 = n_2 = 1$ (cyan) and 3-D RFC method (yellow). With respect to the two reference drawings by the experts, DSCs were found to be 73.1% and 81.3% with HDs of 1.77 mm and 1.62 mm for the RW method; 74.7% and 81.8% with HDs of 1.86 mm and 1.79 mm for the RFC method; and inter-observer agreement was found to be 77.6% and 1.74 mm. Based on the segmentation result, we extracted the distribution of diameter, contrast, signal-to-noise-ratio (SNR), and strong boundary ratio for the 300 images as listed in Table 2. For diameter, small airways are defined as airways with diameter < 2 mm, which is commonly accepted, medium airways are separated to two groups: medium low as 2–2.5 mm defined in

Burgel (2011) and medium high 2.5–5 mm defined in Hashimoto et al. (2005), and large airways are airways with diameter > 5 mm. Contrast is defined as the ratio between mean intensity within lumen area and that within wall. SNR is computed as the ratio between the mean and the standard deviation of the wall intensity. Furthermore, to check the percentage of the weakly defined wall boundary caused by adjacent vessel, we first dilate the segmented airway wall by three pixels, and within the dilated area, the percentage of the dark pixels is computed given that lung parenchyma is dark and vessel is bright and of similar intensity as airway wall. As shown, the test set covers different cases that can be encountered in the initial data.

In addition to region-based evaluation of airway wall surface estimations, we also compared the shape-based accuracy of the estimations using isoperimetric inequality (IPI) measures. Airways are inherently a circular structure, thus local segmentation appearance is expected to favor circular shape rather than spiculated, which provides information for segmentation quality or localized abnormality. Hence, we used IPI as a complementary measure to DSC. IPI is defined as $|4\pi A_i - (\mathcal{L}_i)^2|$, $i = 1, 2$, for inner ($i = 1$) and outer ($i = 2$) surface estimation, respectively, where A_i denotes the area enclosed by the boundary S_i, and $\mathcal{L}_i$ represents the boundary length of the corresponding A_i (for a perfect circle, IPI = 0; larger values indicate deviation from circularity). As a complementary measure to DSC, IPI is a geometric inequality that measures how a closed boundary deviates from a perfect circle, given its enclosed area and the circumference. IPI may also have a role in the CAD systems for quantification of airway thickening or enlargement, once the IPI range for the normal anatomy is defined. In Fig. 10, estimated inner and outer boundaries
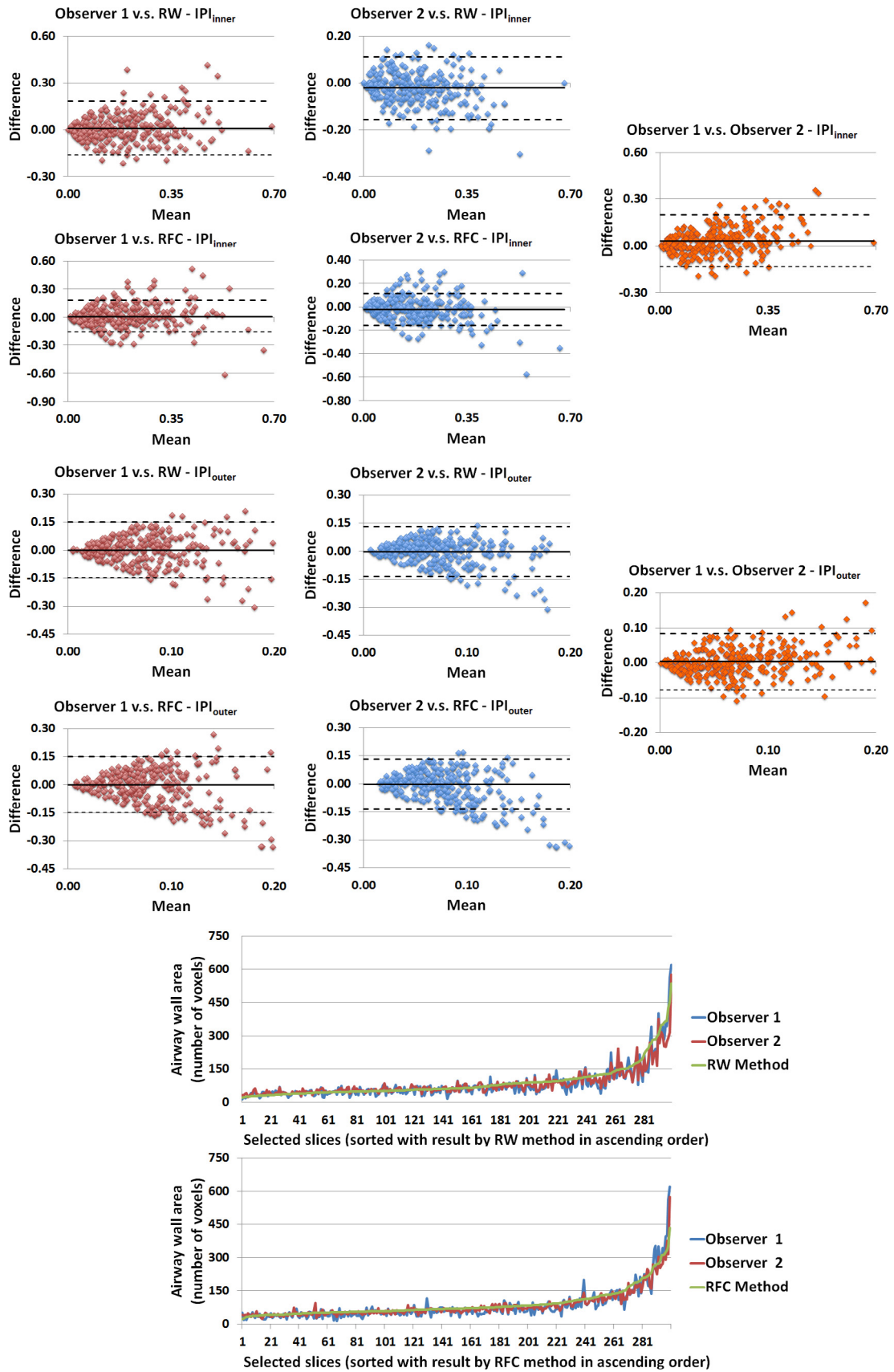
Fig. 10. First four rows show Bland–Altman plots for IPI_inner and IPI_outer measurements across observers and the proposed methods. The last two rows demonstrate the agreement curve of airway wall area measurements by the proposed methods and the two expert observers.

Table 3
Quantitative results for airway wall segmentation.

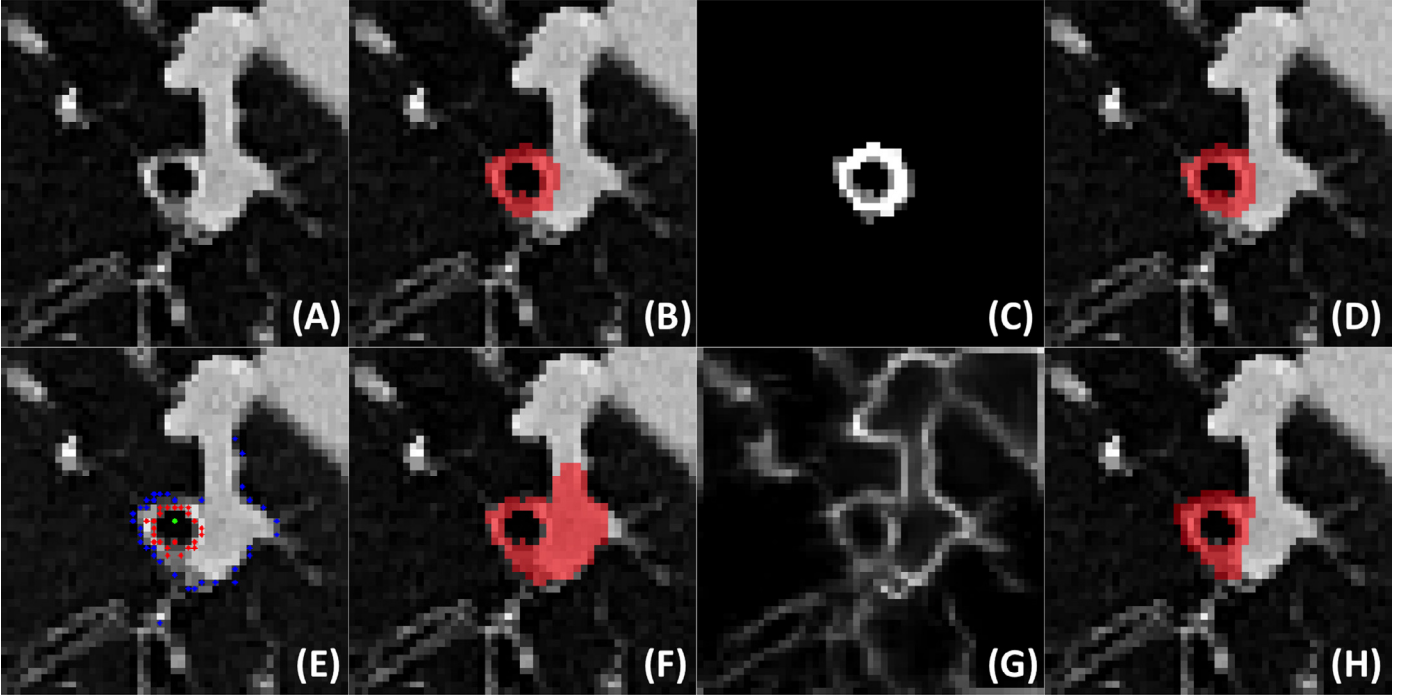|	FWHM	FWHMwithEllipse	PhaseCongruency	RW	RFC
DSCtoObserver1	57.5%	58.6%	63.3%	73.1%	74.7%
DSCtoObserver2	64.5%	65.2%	70.4%	81.3%	81.8%
HDtoObserver1	3.56 mm	2.44 mm	2.26 mm	1.77 mm	1.86 mm
HDtoObserver2	3.35 mm	2.25 mm	2.03 mm	1.62 mm	1.79 mm

Fig. 11. (A) Original image; (B) binary segmentation for RFC method; (C) probability map for RW method; (D) binary segmentation for RW method; (E) edge locations for FWHM method; (F) binary segmentation for FWHM method; (G) edge strength map for phase congruency method; (H) binary segmentation for phase congruency method.

of the airway walls were compared to surrogate truths, provided by Observer 1 and Observer 2, through Bland–Altman plots in columns 1 and 2, respectively. As can be seen, high correlations were obtained when we compared our proposed method to observer evaluations. The third column in the figure indicates the inter-observer agreement for inner and outer wall boundary localization based on IPI measurement (the rate was found to be 75.27%). In the last row, estimated wall areas for all selected slices were compared to surrogate truths, and resulting values were plotted in ascending order. Note that the airway wall areas estimated by the proposed method are highly correlated with observers' evaluations (correlations values of adjusted $R^2 = 0.924$ and $R^2 = 0.931$ were obtained respectively).

3.4. Comparison to widely applied methods

We compared our proposed method with the FWHM and phase congruency methods. The quantitative results are shown in Table 3. As initialization, FWHM method yields DSCs of 57.5% and 64.5% with HDs of 3.56 mm and 3.35 mm, with respect to the surrogate truths; and ellipse fitting promotes the result to 58.6% and 65.2% with HDs of 2.44 mm and 2.25 mm. Phase congruency has better performance at DSCs of 63.3% and 70.4% with HDs of 2.26 mm and 2.03 mm. Inter-observer agreement was 77.6% and 1.74 mm. Fig. 11 shows the wall estimation for an airway (A) for different methods. As shown, FWHM method (E and F) creates false edges, phase congruency (G and H) leaks to neighboring structures due to intensity variation within the walls, while our proposed method of RFC (B) and RW (C and D) successfully avoided leakage and false positives.

3.5. Spatially constrained RW method's sensitivity analysis with respect to the seeds

Because FWHM and ellipse fitting methods were used to *roughly* identify the foreground and background seed locations, it was in our interest to find the sensitivity of the spatially constrained RW method, with respect to changes in the scale parameters n_1 and n_2, which we used to define the new location of the convex surfaces by multiplying the estimated wall thickness with scale parameters n_1 and n_2. The robustness of the proposed method, with regard to seed selection, can be evaluated using different values for n_1 and n_2.

All experimental results were performed on the entire dataset. As stated in the previous section, we have used $n_1 = n_2 = 1$ for our test. Such parameter is a default setting and intuitive (one thickness inside and one thickness outside), hence the selection is not tuned for specific data. Here, during our seed sensitivity test, we have found the "best" results for our dataset when $n_2 = 0.3$. This can be considered as parameter tuning for the candidate dataset. One explanation is that anatomical structures outside the airway walls are complex, so closer to the wall boundary is preferred for the outer seeds. On the other hand, the lumen has a high contrast against neighboring structures, so the inner seeds can be placed further from wall boundary. According to our findings, in the following, we present the results at $n_2 \geq 0.3$ for test under varying inner seeds (on $S_1^{n_1}$), and $n_1 \geq 1.5$ for test under varying outer seeds (on $S_2^{n_2}$).

DSCs were computed for each case, and the result is shown in Fig. 12. As expected, changing the location of inner seeds does not significantly influence the segmentation result (Fig. 12A); while
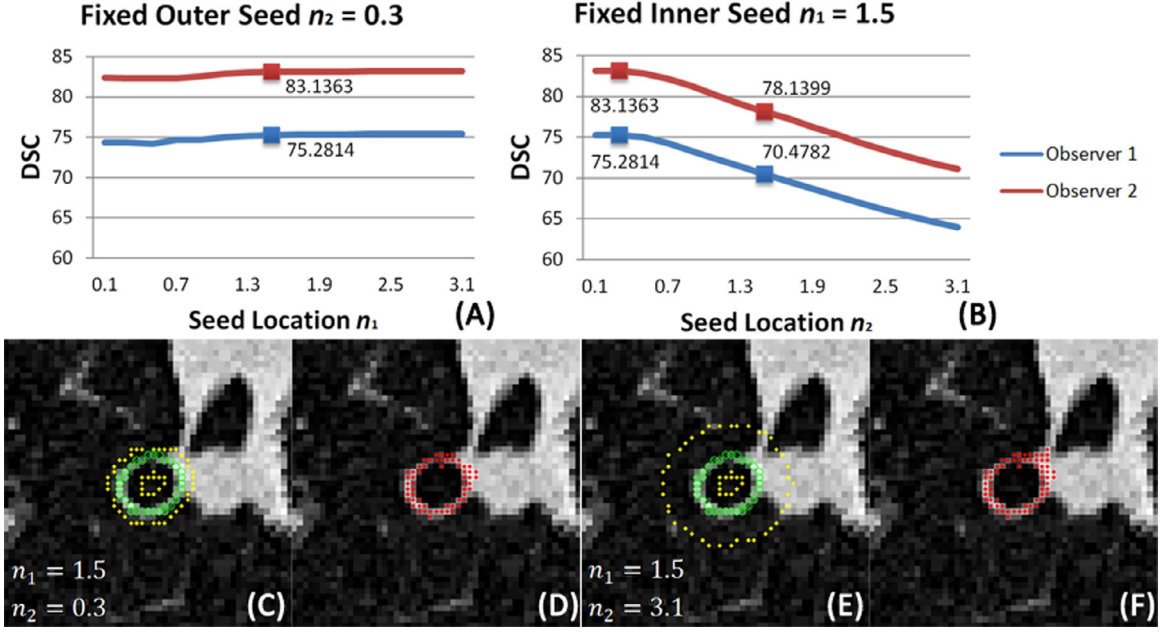
Fig. 12. (A) Dice similarity coefficient with changing inner seeds; (B) Dice similarity coefficient with changing outer seeds; (C), (E) seed locations with two different sets of outer seeds for a specific slice; (D), (F) corresponding segmentation result for the two seed locations.
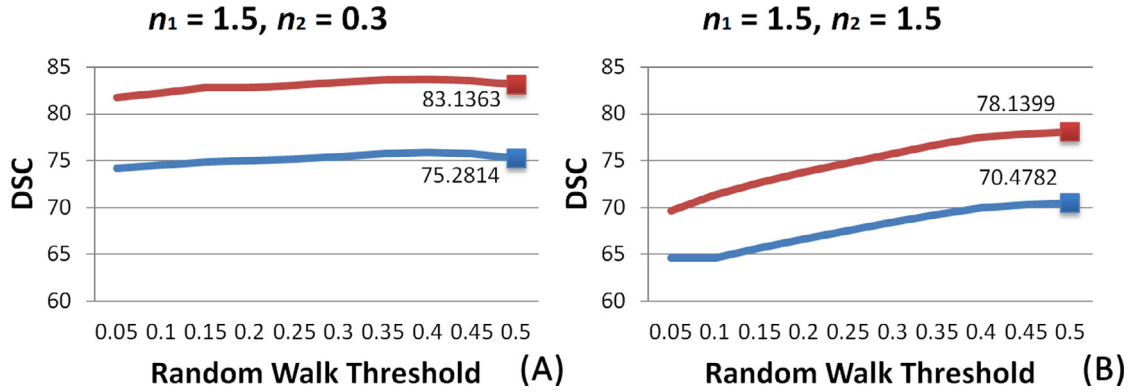

Fig. 13. (A) When spatially constrained RW was used, soft constraints did not change the segmentation results considerably even for large ε change ($n_1 = 1.5$, $n_2 = 0.3$). (B) When outer surface is relaxed ($n_1 = 1.5$, $n_2 = 1.5$), segmentation DSC started to change considerably for $\varepsilon \geq 0.1$. Marked points are from the corresponding values in Fig. 12.

placing the outer background seeds away from the airway wall can decrease the DSC of segmentation (Fig. 12B) since adjacent structures can be falsely included. However, such change is not as dramatic as leakage into neighboring structures. The segmentation result is still constrained within a reasonable margin, when n_2 is large, as shown in Fig. 12C–F.

3.6. Soft constraints in random walks

In this section, we analyze how random walks can be constrained to converge to correct boundaries if spatial constraints are not strict. Analysis of softening spatial constraints and its relation to random walk probabilities in a steady state can show the advantages of using strict spatial constraints in airway wall surface estimations. Consider a set of nodes $\mathcal{F} \subset V$ labeled as foreground, a set of nodes $S_1 \subset V$ labeled as background (on inner surface), and a set of nodes $S_2 \subset V$ labeled as background (on outer surface) such that $\mathcal{F} \cap S_1 = \emptyset$, $\mathcal{F} \cap S_2 = \emptyset$. For any $v \in \mathcal{F}$, $P(v) = 1$, and for any $v \in S_1$ or $v \in S_2$, $P(v) = 0$. For any of the remaining nodes $v \in V \setminus (\mathcal{F} \cup S_1 \cup S_2)$, $P(v) = \sum_{e_{ij} \in E} w_{ij} P(v_j)$. Conventionally, nodes with probability values greater than 0.5 (hard constraint) are classified as foreground. Now, assuming a node is imposed a soft constraint instead of a hard

constraint, the difference between a probability of a node and 0.5 is within a small prescribed range $[-\varepsilon, \varepsilon]$. Then, $|P(v) - 0.5| \leq \varepsilon$ for $v \in V \setminus (\mathcal{F} \cup S_1 \cup S_2)$. By imposing soft constraints, the RW can be considered as a minimization problem,

$$\min \sum_{e_{ij} \in E} w_{ij} |P(v_i) - P(v_j)|^2 + \sum_{v_i \in V \setminus (\mathcal{F} \cup S_1 \cup S_2)} \lambda_i |P(v_i) - 0.5|^2 \quad (11)$$

such that $|P(v) - 0.5| \leq \varepsilon$ for $v \in V \setminus (\mathcal{F} \cup S_1 \cup S_2)$, and $P(v) = 0$ for $v \in S_1$ or $v \in S_2$, and λ controls the weight of the nodes with soft constraints. Detailed solution of this quadratic problem is outside the scope of this paper. However, by varying the ε value in the same segmentation settings, one can analyze the effect of the spatial constraints on the RW. Fig. 13 shows DSC values of the proposed method with respect to the different threshold values for the RW (i.e., soft constraints). As can be seen from Fig. 13A, large changes in ε do not affect the performance of the proposed segmentation algorithm if spatial constraints are provided ($n_1 = 1.5$, $n_2 = 0.3$). If the outer surface S_2 is relaxed ($n_1 = 1.5$, $n_2 = 1.5$), then $\varepsilon \leq 0.1$ (i.e., $P(v)$ down to 0.4 threshold value) yields reasonably good DSC values (Fig. 13B). Note that relaxing S_1 does not affect the segmentation results due to high contrast difference between lumen and airway inner wall, as mentioned in the previous subsection. These findings indicate that

Table 4
Evaluation measures for the 20 cases in the test set.

	Branch count	Branch detected (%)	Tree length (cm)	Tree length detected (%)	Leakage count	Leakage volume (mm³)	False positive rate (%)
CASE21	98	49.2	54.8	49.6	6	18.9	0.28
CASE22	210	54.3	160.6	48.6	7	26.5	0.19
CASE23	189	66.5	134.2	51.6	8	8.9	0.07
CASE24	113	60.8	88.3	54.3	27	66.7	0.45
CASE25	122	52.1	96.2	38.2	4	21.1	0.15
CASE26	31	38.8	20.7	31.5	17	4717.9	119.59
CASE27	71	70.3	50.3	62.1	32	368.3	4.20
CASE28	72	58.5	49.3	44.9	0	0.0	0.00
CASE29	104	56.5	70.7	51.2	5	14.8	0.19
CASE30	98	50.3	67.7	44.3	1	4.3	0.06
CASE31	113	52.8	76.5	43.6	4	261.8	2.55
CASE32	106	45.5	85.5	39.2	4	130.0	1.15
CASE33	107	63.7	80.4	54.7	1	3.2	0.06
CASE34	280	61.1	188.8	52.8	13	42.8	0.21
CASE35	138	40.1	88.0	28.4	4	1.8	0.01
CASE36	114	31.3	115.1	27.9	0	0.0	0.00
CASE37	72	38.9	57.4	32.3	1	0.4	< 0.01
CASE38	40	40.8	29.6	44.6	2	10.1	0.17
CASE39	184	35.4	137.8	33.7	10	68.3	0.63
CASE40	214	55.0	170.0	43.9	35	1258.1	5.71
Mean	128.7	51.7	94.8	44.5	8.6	121.3	0.85
Std. dev.	60.3	10.8	44.7	9.4	10.7	292.2	1.59
Min	40	31.3	29.6	27.9	0	0.0	0.00
1st quartile	98	43.15	62.55	38.7	1.5	3.75	0.06
Median	113	52.5	85.5	44.6	4	18.9	0.19
3rd quartile	161	59.65	124.65	51.4	9	67.5	0.54
Max	280	70.3	188.8	62.1	35	1258.1	5.71

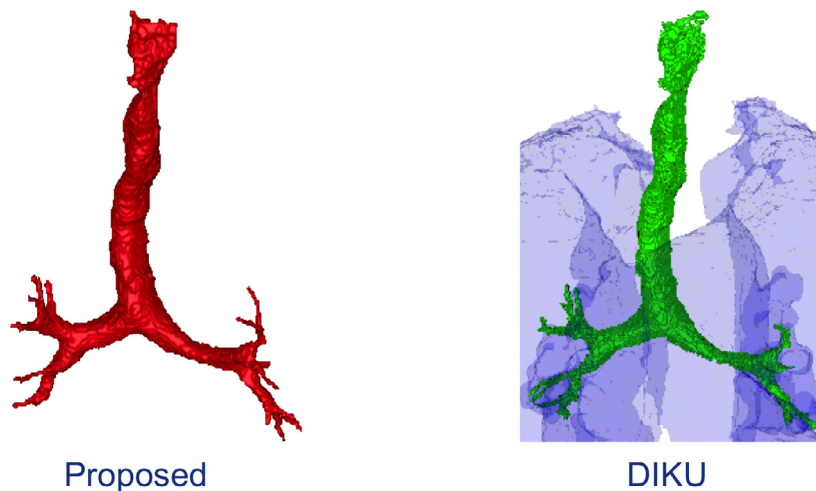**Proposed**   **DIKU**

Fig. 14. Airway segmentation for CASE26 by proposed method and reference result from DIKU.

the spatially constrained RW is a stable and robust method for finding boundaries of inner and outer surfaces, and sensitivity of the boundary localization is high even when spatial constraints are not strict.

4. Discussion and conclusion

One question that arises is which of the 2-D (pseudo-3D) and 3-D techniques better suits the task of airway wall estimation. Although 3-D implementation performs better in branching areas and is more efficient in generating the 3-D tree structure, routine clinical analysis of airways often requires a pseudo 3-D implementation to measure airway dimensions in-plane and may be in selected image slices only. We found no statistically significant difference in segmentation results of both methods ($p = 0.32$ and $p = 0.42$ for RFC and RW based methods, respectively); however, 3-D RFC is faster compared to the RW based method.

It may be possible to use the phase congruency method to define inner and outer surfaces instead of FWHM method, for identi-

fying background and foreground seeds. Comparison of FWHM and phase congruency methods in the literature reveals that phase congruency may identify inner and outer surfaces of airway walls better, hence, seeding locations may be more precise; however, an accurate comparison of these methods, within the spatially constrained RW method, and the computational burden analysis, are left as an extension of this study.

In the evaluation step, we used EXACT'09 data sets to compare our results with the state-of-the-art methods. Although our method is likely to be suitable for analyzing all images from the EXACT'09 challenge, we will extend our evaluations with the data sets of different airway diseases with high and low resolution CT scans as a feasibility study for our ongoing clinical research.

One of the difficulties in proposing a general segmentation approach for airway and airway walls is reproducibility of the research due to unavailability of gold standard results. Although phantom studies could provide some insights about the robustness of the
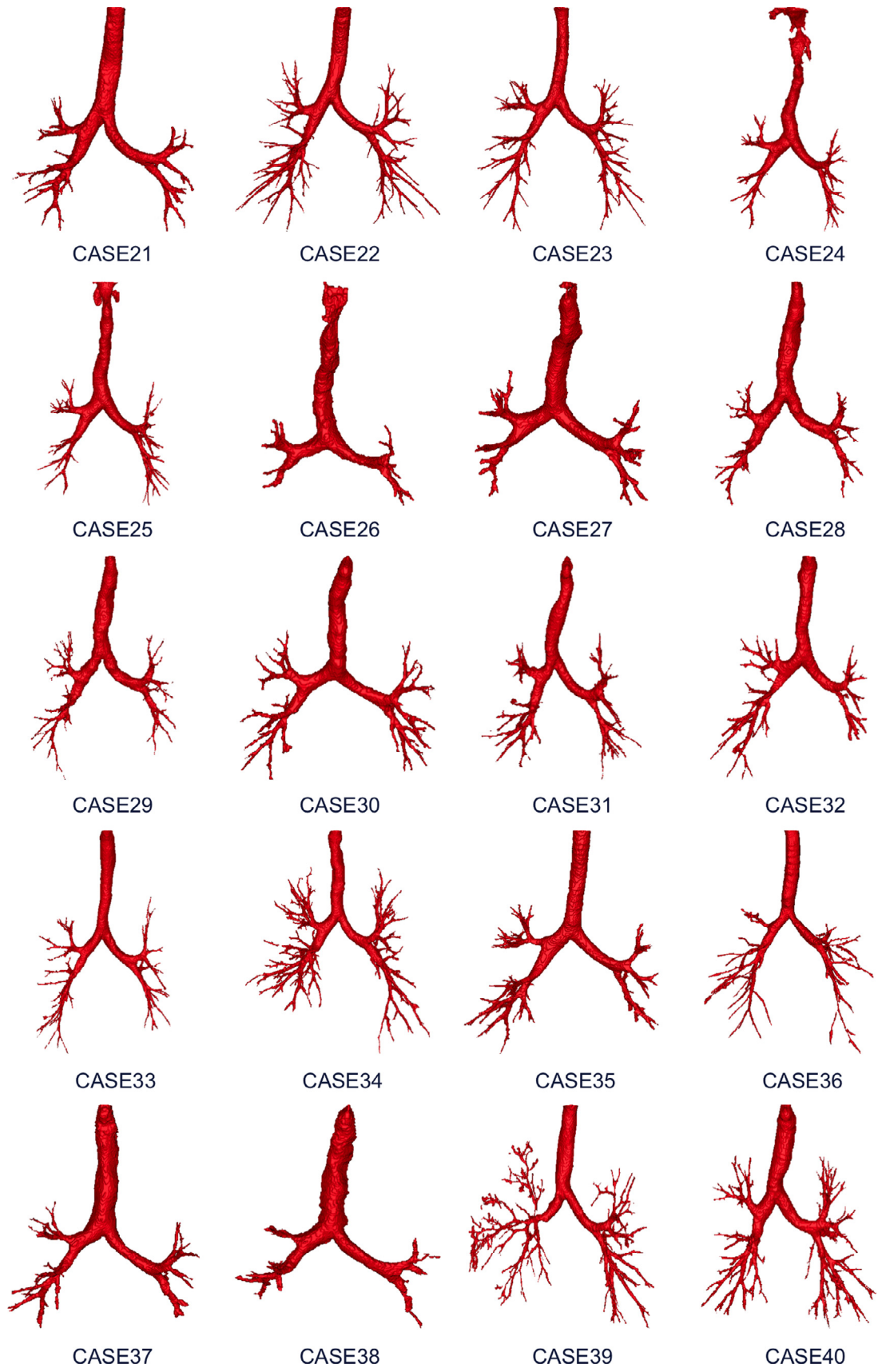
Fig. 15. Segmentation results for the twenty cases in the test set.

methods, natural variability of the human anatomy is not reflected in phantom designs. Regarding this issue, a very recent work of Kohlberger et al. (2012) showed a generic learning approach based on a novel space of segmentation features, which can be trained to predict the overlap error and dice coefficient of arbitrary organ segmentation without knowing "the ground truth delineation". Arguably, it may be possible in the near future to evaluate image segmentation algorithms without having a reference truth (Bagci et al., 2013a; 2013c), thus robustness and reproducibility of the airway and airway wall segmentation methods.

There may be other alternatives for airway wall segmentation. Two of them we intend to investigate are Iterative RFC (IRFC), and synergistically combined IRFC and Graph Cut (GC). Given accurate seed placement in appropriate background components, IRFC is known to perform better than RFC in accuracy and speed. Recently IRFC and GC have been applied alternately have been shown to effectively combine the speed and robustness properties of IRFC with the boundary smoothness characteristics of GC to yield better segmentations (Ciesielski et al., 2013).

In conclusion, we designed and developed novel algorithms to accurately segment lung airways and measure airway wall thickness as a means to map lung anatomy and identify areas of disease, such as cancer, infection, and immune disease. Our approach was based on the fuzzy connectedness theory for precise segmentation of the airway lumen, and a spatially constrained Markov random walk and relative fuzzy connectedness methods to estimate the airway wall surfaces. For lumen segmentation, the proposed method combines vesselness and gray-scale morphological reconstruction with FC facilitating robust and reliable region growth along thin airway structures. By incorporating multiple features to identify airway tree at different levels of scales, the algorithm adapts and governs the fuzzy segmentation process and captures airways under different pathological and imaging conditions more robustly in the presence of noise and other artifacts. The proposed methods are fully automated with automatic seed identification algorithms and the performance of the methods has been qualitatively and quantitatively evaluated on human pulmonary CT images from diverse subjects. Optimization techniques have been employed to extract the skeletons of airways and then an automatic seeding procedure based on FWHM and ellipse fitting was designed in order to spatially constrain Markov random walk. In the meantime, three surfaces for airway wall estimation were first roughly estimated, and they were used as seed sets for relative fuzzy connectedness computation. Both 2-D and 3-D methods performed similarly with high accuracy. Results demonstrated that our airway analysis platform gave a better identification of the inner and outer airway surfaces than the widely applied methods.

Acknowledgments

Appendix A

Table 4 lists the quantitative results we received from the EXACT'09 organizer for twenty cases in the test set. Note that for CASE26, due to an uploading error, a huge amount of false positive of 119.59% is reported. Hence, we identified it as an error of calculation from the organizer's side and excluded it from the final result. For reference, Fig. 14 illustrates the binary airway segmentation of CASE26 from the proposed method and reference DIKU method. It can be observed that the two methods have relatively similar performance (even more detection rate in airway tree), and DIKU method have 50% tree length detected and 0.0% false positive rate. Furthermore,

for completeness of the paper, all the 20 cases' segmentation results are presented in Fig. 15.

References

Amirav, I., Kramer, S.S., Grunstein, M.M., Hoffman, E.A., 1993. Assessment of methacholine-induced airway constriction by ultrafast high-resolution computed tomography. J. Appl. Physiol. 75 (5), 2239–2250.

Aykac, D., Hoffman, E.A., McLennan, G., Reinhardt, J.M., 2003. Segmentation and analysis of the human airway tree from three-dimensional X-ray CT images. IEEE Trans. Med. Imaging 22 (8), 940–950.

Bagci, U., Bray, M., Caban, J., Yao, J., Mollura, D.J., 2012. Computer-assisted detection of infectious lung diseases: a review. Comput. Med. Imaging Graphics 36 (1), 72–84.

Bagci, U., Foster, B., Miller-Jaster, K., Luna, B., Dey, B., Bishai, W., Jonsson, C., Jain, S., Mollura, D., 2013. A computational pipeline for quantification of pulmonary infections in small animal models using serial PET-CT imaging. EJNMMI Res. 3 (1), 55.

Bagci, U., Kramer-Marek, G., Mollura, D., 2013. Automated computer quantification of breast cancer in small-animal models using PET-guided MR image co-segmentation. EJNMMI Res. 3 (1), 49.

Bagci, U., Kramer-Marek, G., Mollura, D., 2013. Automated computer quantification of breast cancer in small-animal models using PET-guided MR image co-segmentation. EJNMMI Res. 3 (1), 49.

Bagci, U., Udupa, J., Yao, J., Mollura, D., 2012. Co-segmentation of functional and anatomical images. In: Medical Image Computing and Computer-Assisted Intervention (MICCAI) 2012. In: Lecture Notes in Computer Science, 7512, pp. 459–467.

Bagci, U., Udupa, J.K., Mendhiratta, N., Foster, B., Xu, Z., Yao, J., Chen, X., Mollura, D.J., 2013. Joint segmentation of anatomical and functional images: Applications in quantification of lesions from PET, PET-CT, MRI-PET, and MRI-PET-CT images. Med. Image Anal. 17 (8), 929–945.

Burgel, P.-R., 2011. The role of small airways in obstructive airway diseases. Eur. Respir. Rev. 20 (119), 023–033.

Cheng, M., Zhang, G., 2011. Connectedness of random walk segmentation. IEEE Trans. Pattern Anal. Mach. Intell. 33 (1), 200–202.

Ciesielski, K.C., Miranda, P.A., Falco, A.X., Udupa, J.K., 2013. Joint graph cut and relative fuzzy connectedness image segmentation algorithm. Med. Image Anal. 17 (8), 1046–1057.

Estepar, R.S., Washko, G.G., Silverman, E.K., Reilly, J.J., Kikinis, R., Westin, C.F., 2006. Accurate airway wall estimation using phase congruency. In: Medical Image Computing and Computer-Assisted Intervention (MICCAI) 2006. In: LNCS, 4191, pp. 125–134.

Fetita, C., Ortner, M., Brillet, P.-Y., Prteux, F., Grenier, P., 2009. A morphological-aggregative approach for 3D segmentation of pulmonary airways from generic MSCT acquisitions. In: Second International Workshop on Pulmonary Image Analysis, pp. 215–226.

Frangi, A., Niessen, W., Vincken, K., Viergever, M., 1998. Multiscale vessel enhancement filtering. In: Medical Image Computing and Computer-Assisted Intervention (MICCAI) 1998. In: LNCS, 1496, pp. 130–137.

Grady, L., 2006. Random walks for image segmentation. IEEE Trans. Pattern Anal. Mach. Intell. 28 (11), 1768–1783.

Gu, S., Fuhrman, C., Meng, X., Siegfried, J.M., Gur, D., Leader, J.K., Sciurba, F.C., Pu, J., 2013. Computerized identification of airway wall in CT examinations using a 3D active surface evolution approach. Med. Image Anal. 17 (3), 283–296.

Hansell, D.M., Bankier, A.A., MacMahon, H., McLoud, T.C., Mller, N.L., Remy, J., 2008. Fleischner society: glossary of terms for thoracic imaging. Radiology 246 (3), 697–722.

Hashimoto, M., Tanaka, H., Abe, S., 2005. Quantitative analysis of bronchial wall vascularity in the medium and small airways of patients with asthma and COPD. Chest 127 (3), 965–972.

Ibanez, L., Schroeder, W., Ng, L., Cates, J.1-930934-15-7, 2005. The ITK Software Guide, second ed. Kitware, Inc.

Kohlberger, T., Singh, V., Alvino, C., Bahlmann, C., Grady, L., 2012. Evaluating segmentation error without ground truth. Med. Image Comput. Comput. Assist. Intervention 7510, 528–536.

Liu, X., Chen, D., Tawhai, M., Wu, X., Hoffman, E., Sonka, M., 2013. Optimal graph search based segmentation of airway tree double surfaces across bifurcations. IEEE Trans. Med. Imaging 32 (3), 493–510.

Lo, P., van Ginneken, B., Reinhardt, J., Yavarna, T., de Jong, P., Irving, B., Fetita, C., Ortner, M., Pinho, R., Sijbers, J., Feuerstein, M., Fabijanska, A., Bauer, C., Beichel, R., Mendoza, C., Wiemker, R., Lee, J., Reeves, A., Born, S., Weinheimer, O., van Rikxoort, E., Tschirren, J., Mori, K., Odry, B., Naidich, D., Hartmann, I., Hoffman, E., Prokop, M., Pedersen, J., de Bruijne, M., 2012. Extraction of airways from CT (EXACT'09). IEEE Trans. Med. Imaging 31 (11), 2093–2107.

Lo, P., Sporring, J., Ashraf, H., Pedersen, J.J.H., de Bruijne, M., 2010. Vessel-guided airway tree segmentation: a voxel classification approach. Med. Image Anal. 14 (4), 527–538.

Lo, P., Sporring, J., de Bruijne, M., 2009. Multiscale vessel-guided airway tree segmentation. In: Second International Workshop on Pulmonary Image Analysis, pp. 323–332.

Okazawa, M., Müller, N., McNamara, A.E., Child, S., Verburgt, L., Paré, P.D., 1996. Human airway narrowing measured using high resolution computed tomography. Am. J. Respir. Crit. Care Med. 154 (5), 1557–1562.

Ortner, M., Fetita, C., Brillet, P.-Y., Prêteux, F., Grenier, P., 2011. Surface modeling and segmentation of the 3D airway wall in MSCT. In: Proc. SPIE 7964, Medical Imaging 2011: Visualization, Image-Guided Procedures, and Modeling, 79640O doi:10.1117/12.877521.

Petersen, J., Nielsen, M., Lo, P., Saghir, Z., Dirksen, A., De Bruijne, M., 2011. Optimal graph based segmentation using flow lines with application to airway wall segmentation. In: International Conference on Information Processing in Medical Imaging (IPMI) 2011, pp. 49–60.

Pinho, R., Luyckx, S., Sijbers, J., 2009. Robust region growing based intrathoracic airway tree segmentation. In: Second International Workshop on Pulmonary Image Analysis, pp. 261–271.

Pu, J., Gu, S., Liu, S., Zhu, S., Wilson, D., Siegfried, J.M., Gur, D., 2012. CT based computerized identification and analysis of human airways: a review. Med. Phys. 39 (5), 2603–2616.

Reinhardt, J.M., D'Souza, N.D., Hoffman, E.A., 1997. Accurate measurement of intrathoracic airways. IEEE Trans. Med. Imaging 16 (6), 820–827.

Saba, O.I., Hoffman, E.A., Reinhardt, J.M., 2003. Maximizing quantitative accuracy of lung airway lumen and wall measures obtained from X-ray CT imaging. J. Appl. Physiol. 95 (3), 1063–1075.

Saha, P.K., Udupa, J.K., 2001. Fuzzy connected object delineation: Axiomatic path strength definition and the case of multiple seeds. Comput. Vision Image Understanding 83 (3), 275–295.

Sonka, M., Park, W., Hoffman, E.A., 1996. Rule-based detection of intrathoracic airway trees. IEEE Trans. Med. Imaging 15 (3), 314–326.

Udupa, J.K., Samarasekera, S., 1996. Fuzzy connectedness and object definition: theory, algorithms, and applications in image segmentation. CVGIP: Graphical Model & Image Process. 58 (3), 246–261.

Xu, Z., Bagci, U., Foster, B., Mansoor, A., Mollura, D., 2013. Spatially constrained random walk approach for accurate estimation of airway wall surfaces. In: Medical Image Computing and Computer-Assisted Intervention – MICCAI 2013. In: Lecture Notes in Computer Science, 8150. Springer, Berlin, Heidelberg, pp. 559–566.

Xu, Z., Bagci, U., Foster, B., Mollura, D.J., 2013. A hybrid multi-scale approach to automatic airway tree segmentation from CT scans. In: IEEE International Symposium on Biomedical Imaging (ISBI) 2013, pp. 1308–1311.

Xu, Z., Zhao, F., Bhagalia, R., Das, B., 2012. Generic rebooting scheme and model-based probabilistic pruning algorithm for tree-like structure tracking. In: IEEE International Symposium on Biomedical Imaging (ISBI) 2012, pp. 796–799.